



**HAL**  
open science

## A decision aid for the port placement problem in robot-assisted hysterectomy

Mohammad R Maddah, Jean-Marc Classe, Isabelle Jaffre, Keith A Watson, Katherine S Lin, Damien Chablat, Cédric Dumas, Caroline G.L. Cao

► **To cite this version:**

Mohammad R Maddah, Jean-Marc Classe, Isabelle Jaffre, Keith A Watson, Katherine S Lin, et al.. A decision aid for the port placement problem in robot-assisted hysterectomy. *Laparoscopic, Endoscopic and Robotic Surgery*, 2023, 6 (2), pp.43-56. 10.1016/j.lers.2023.05.002 . hal-04113365

**HAL Id: hal-04113365**

**<https://hal.science/hal-04113365v1>**

Submitted on 1 Jun 2023

**HAL** is a multi-disciplinary open access archive for the deposit and dissemination of scientific research documents, whether they are published or not. The documents may come from teaching and research institutions in France or abroad, or from public or private research centers.

L'archive ouverte pluridisciplinaire **HAL**, est destinée au dépôt et à la diffusion de documents scientifiques de niveau recherche, publiés ou non, émanant des établissements d'enseignement et de recherche français ou étrangers, des laboratoires publics ou privés.

## A decision aid for the port placement problem in robot-assisted hysterectomy

Mohammad R. Maddah<sup>a, b, c</sup>, Jean-Marc Classe<sup>d</sup>, Isabelle Jaffre<sup>d</sup>, Keith A. Watson<sup>e</sup>, Katherine S. Lin<sup>e</sup>, Damien Chablat<sup>c</sup>, Cedric Dumas<sup>b, c</sup>, Caroline G.L. Cao<sup>a, f, g, h, \*</sup>

<sup>a</sup> Department of Biomedical, Industrial, and Human Factors Engineering, Wright State University, 3640 Colonel Glenn Hwy, Dayton, OH, USA

<sup>b</sup> Department of Automatique, Productique et Informatique, IMT Atlantique, 4 Rue Alfred Kastler, Nantes, France

<sup>c</sup> Laboratoire des Sciences Du Numerique de Nantes (LS2N), 2 Chemin de La Houssinière, Nantes, France

<sup>d</sup> Centre René Gauducheau ICO Institut de Cancerologie de L'Ouest, BD Professeur Jacques Monod, Saint-Herblain, France

<sup>e</sup> Brethren Center for Surgical Advancement in Robotics and Minimally Invasive Surgery, Miami Valley Hospital, One Wyoming Street, Dayton, OH, USA

<sup>f</sup> Department of Computer Science, IMT Atlantique, Technopole Brest-Iroise, Brest, France

<sup>g</sup> Laboratoire des Sciences et Techniques de L'information de La Communication et de La Connaissance (Lab-STICC), Technopole Brest-Iroise, Brest, France

<sup>h</sup> Future Industries Institute, STEM, University of South Australia, Mawson Lakes Blvd, Mawson Lakes, Australia

### ARTICLE INFO

#### Article history:

Received 6 April 2023

Received in revised form

2 May 2023

Accepted 15 May 2023

Available online xxx

Edited by Qingjie Zeng

#### Keywords:

Optimization

Planning tool

Patient model

Robotic hysterectomy

### ABSTRACT

**Objective:** In robot-assisted minimally invasive surgery, proper port positioning ensures that surgical tools have adequate access to the surgical site and avoids mid-surgery collisions of robotic arms. To date, several guidelines have been proposed for more accurate port placement. However, challenges remain due to variations in patient morphology, anatomy, and, in particular, organ displacement due to insufflation in certain laparoscopic procedures. The objective of this study was to design and develop a decision aid for optimal port placement in robot-assisted hysterectomy that accounts for patient variability and organ displacement due to insufflation.

**Methods:** Three components were constructed: a robot model, a patient-specific model, and an optimization algorithm. The three components were integrated, and the system was verified using four different patients who underwent robotic hysterectomy. Once verified, two expert surgeons were asked to evaluate the decision aid for face and construct validity. A usability test was conducted using a torso phantom with target organs located in three different locations. Two expert surgeons performed a simulated hysterectomy task with and without the decision aid to evaluate performance and satisfaction.

**Results:** The optimization algorithm was sensitive to individual differences in anatomy in the four patients. Expert surgeons successfully established face and construct validity. Usability test results showed a 28%–40% reduction in time to task completion with the optimized ports compared to expert-determined port locations without using the decision aid.

**Conclusions:** The decision aid, based on an individualized patient-specific model, robot model, and optimization algorithm, was shown to be effective at addressing the challenges of displaced organs due to insufflation in robot-assisted hysterectomy. The face and construct validity of the decision aid was established by expert surgeons, while efficiency gains in task performance were demonstrated experimentally.

© 2023 Zhejiang University. Publishing services by Elsevier B.V. on behalf of KeAi Communications Co. Ltd. This is an open access article under the CC BY-NC-ND license (<http://creativecommons.org/licenses/by-nc-nd/4.0/>).

## 1. Introduction

In robotic minimally invasive surgery (MIS) performed using the da Vinci Surgical System,<sup>1</sup> three or four surgical instruments,

including an endoscope to see inside the patient, are inserted into a patient's body through small entry ports to remotely perform the surgical operation.<sup>1,2</sup> The entry ports on the patient's body serve as pivot points for the instruments that are attached to the robot arms and controlled by the surgeon seated at the console.<sup>2</sup> Therefore, the entry port positions, or port placement, play a significant role in the success of the operation. The robot manufacturer<sup>1</sup> provides instructions for standard port placement in different MIS robotic

\* Corresponding author: Department of Computer Science, IMT Atlantique, Technopole Brest-Iroise, Brest, France.

E-mail address: [cao.caroline@gmail.com](mailto:cao.caroline@gmail.com) (C.G.L. Cao).

<https://doi.org/10.1016/j.lers.2023.05.002>

2468-9009/© 2023 Zhejiang University. Publishing services by Elsevier B.V. on behalf of KeAi Communications Co. Ltd. This is an open access article under the CC BY-NC-ND license (<http://creativecommons.org/licenses/by-nc-nd/4.0/>).

procedures.<sup>1</sup> However, surgeons frequently complain about inadequate guidelines and lack of support for adapting the port placement plan to individual patients.<sup>3</sup> Unreachable targets and mid-surgery collisions of robotic arms are major issues resulting from nonoptimal placement of the ports in MIS robotic procedures.<sup>4</sup>

In practice, surgeons estimate port locations based on the patient's torso size and external landmarks, such as nipples, sternum, and umbilicus, after insufflation.<sup>5,6</sup> As body sizes and target organ positions are different from patient to patient, good port placement requires adjustments according to individual patients. Additionally, the outer shape of the patient's abdomen and the target organ position are changed by the insufflation process,<sup>7,8</sup> exacerbating any estimation error.

Several solutions for the port-placement problem in MIS procedures have been proposed.<sup>4,9</sup> These solutions used either a patient model (a 3D shape of the patient's body) or a robot kinematic model (the robot arms' configuration and positions relative to the patient) to determine the optimal positions of the entry ports.<sup>10</sup> However, the patient and the robot models were simple representations of the patient's body and the robot arms.<sup>4,10–12</sup> In another application, preoperative CT images were used to create a 3D patient model for more accurate port placement in coronary artery bypass grafting surgery.<sup>5,9</sup> However, this approach would require the preoperative (i.e., before insufflation) 3D model to be registered on the inflated abdomen intraoperatively,<sup>13</sup> as well as to adjust for organ shape and position changes after insufflation.<sup>8,14,15</sup> Others have used kinematic analysis to model the manipulators in MIS robotic procedures, defining a performance index to measure the robot arm performance in manipulating a target inside a small box.<sup>16,17</sup>

Most existing port-placement guidance systems are limited to MIS procedures such as coronary artery bypass surgeries<sup>4,8,18</sup> that do not involve insufflation of patients. They rely on preoperative medical images, ignoring possible changes in body shape and organ displacements due to insufflation.<sup>5,9</sup> Here, we describe the development and evaluation of a new decision-aid for optimal port placement in robotic hysterectomy that takes into account the aforementioned issues related to insufflation and accommodates individual patient characteristics.

## 2. Methods

The decision-aid consists of a patient-specific model, a robot model, and an optimization algorithm (or decision-making unit) (Fig. 1). The patient-specific model is a post-insufflation 3D model of the patient abdomen that includes all the changes in the patient body due to insufflation. The robot model is the robotic arm configuration related to the patient-specific model.<sup>19</sup> The optimization algorithm determines the location of the entry ports that minimize collisions between surgical instruments inside the patient while maximizing an efficiency index during surgery.<sup>10</sup>

### 2.1. Patient-specific model development

While it is possible to use portable CT scanners (e.g., mobile C-arm) to acquire 3D patient-specific models in the operating room, this approach is expensive and complex,<sup>20,21</sup> and not available in all operating rooms. We propose a method in which two different 3D models of the patient abdominal cavity, before and after insufflation, were created and referred to as internal and external models, respectively. The internal and external models were then superimposed to create the patient-specific model (3D mesh), which included the changes in the outer shape of the abdomen and the target organ position after insufflation.

First, the internal model was constructed from preoperative CT medical images using the insight toolkit (ITK), visualization toolkit and ITK-SNAP segmentation tools<sup>22–26</sup> (Fig. 2). The target organ (i.e., uterus) location in the internal model was updated using displacement data obtained from a previous study that employed animal bodies (sows) to measure the displacement of organs under intra-abdominal pressure during insufflation.<sup>8</sup> Next, the external model was constructed using 3D scans of the expanded abdomen after insufflation. Several different methods have been investigated to track and monitor the deformation of the abdominal wall during insufflation.<sup>13,27</sup> However, to avoid the complexity of these methods, advanced 3D scanners, such as Artec or Kinect, can be used to capture the abdominal surface during insufflation.<sup>28–30</sup> In this study, we used a Kinect camera that was easily mounted above the patient to accurately image the abdomen during insufflation

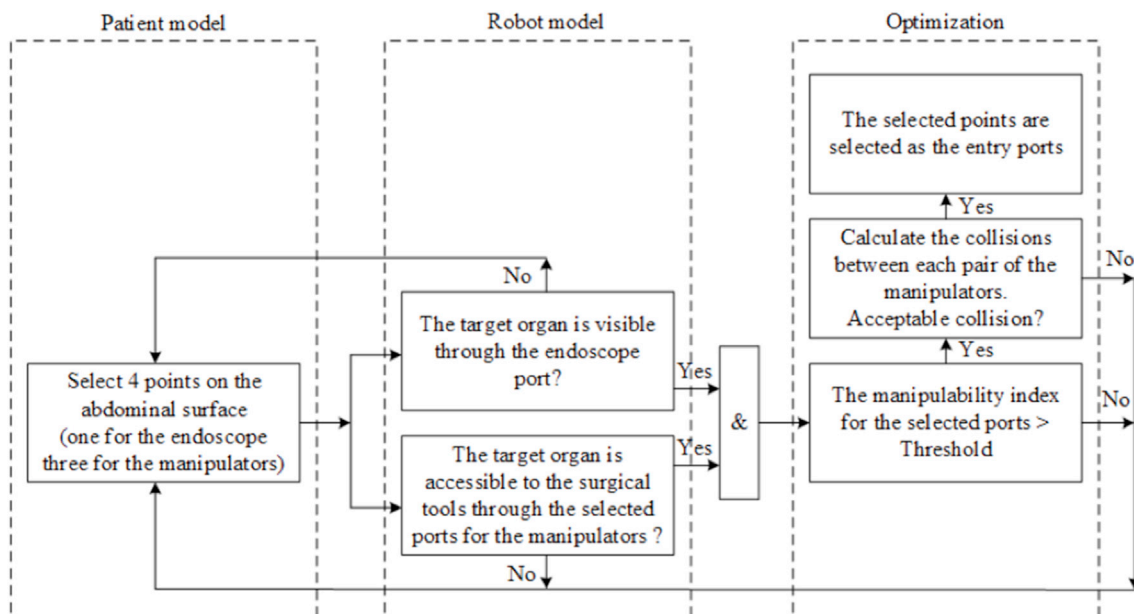
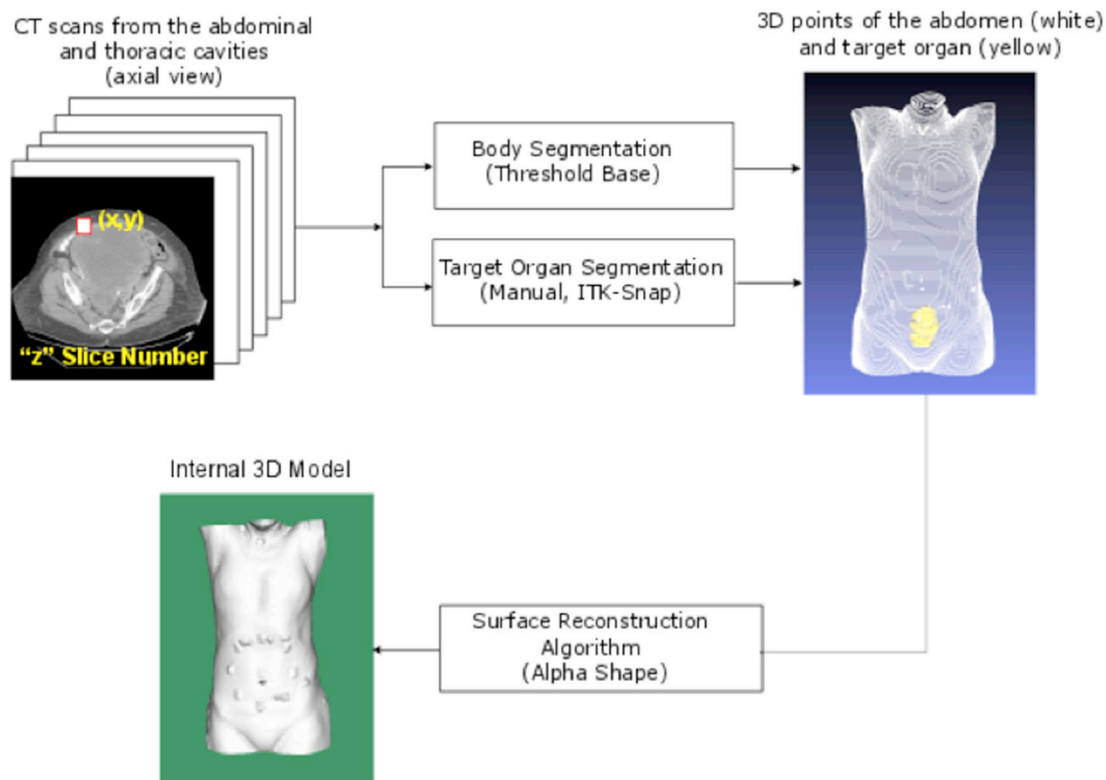


Fig. 1 Major components of the port placement decision aid for robot-assisted surgical procedures



**Fig. 2** Workflow for the construction of the patient's 3D internal model

Target shape (uterus) and abdomen boundaries in CT images are segmented using ITK-SNAP (top-left). 3D pixels of the target organ and the abdomen are converted to 3D points based on their positions in the CT slices (by ITK software). The abdomen is depicted in white, and the target organ is depicted in yellow (top right). Finally, the Alpha shape surface reconstruction algorithm was used to create a 3D shape of the abdomen (including the target organ) called the internal model (bottom).

(Fig. 3).<sup>29,31</sup> The 3D points generated from the inflated abdomen in front of the Kinect camera were fed into a surface construction algorithm to create the external model<sup>25</sup> (Fig. 4).

A least-square method was applied to superimpose the external model on the internal model to construct the patient-specific

model.<sup>32</sup> Four points on the internal model were assumed to be fixed during insufflation: on the anterior superior iliac and the tenth rib of the thoracic cage (Fig. 5). The points on the front edges of the rib cage and the pelvic bone were located and segmented in the CT images. These points were also located and marked on the

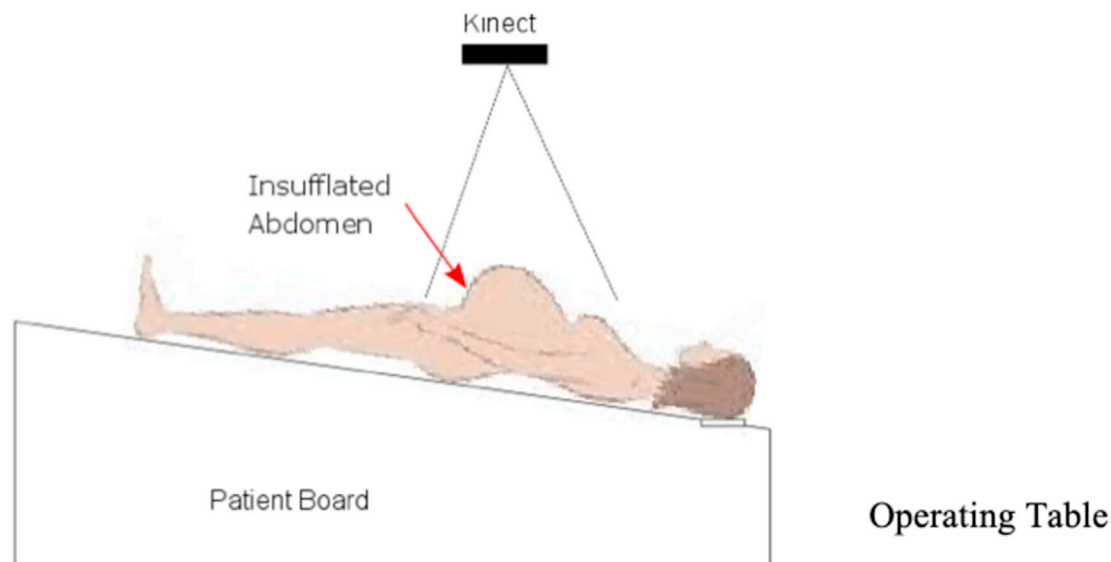


**Fig. 3** Imaging the abdominal surface during insufflation

A Kinect camera is mounted directly above the patient on the operating table. The patient's inflated abdomen (due to insufflation) is imaged as 3D points that are used for constructing the external model.

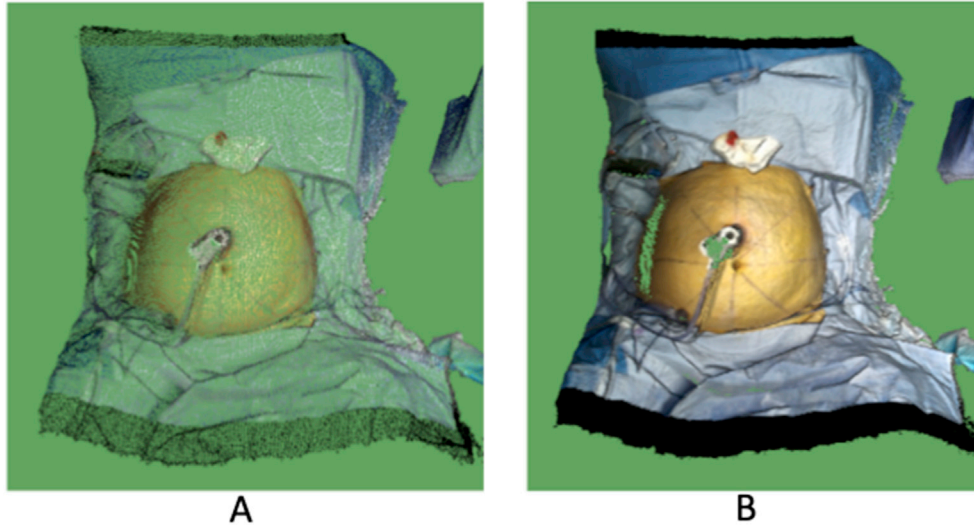


**Fig. 4** The creation of an external model based on a surface construction algorithm  
 A, Example of 3D points of the patient's insufflated abdomen, captured by the Kinect camera. B, Example of the patient external model constructed from the 3D points using a surface reconstruction algorithm (Alpha Shape).

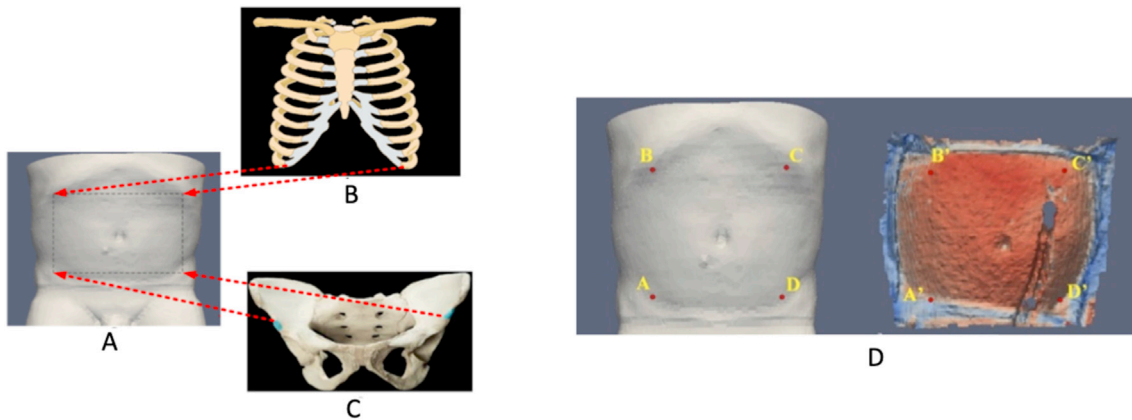


**Fig. 5** Construction of a patient-specific model by aligning four anatomical landmarks on the internal and external models using a least-square method  
 A, The four landmarks are shown on the internal model. B, Two points on the tenth rib. C, Two points on the anterior superior iliac. D, The corresponding points on the internal (from preoperative CT slices) and external (from Kinect 3D points) models.

abdominal surface by the surgeon for detection by the Kinect sensor. The result of aligning the internal and external models is the patient-specific model (Fig. 6). This work was performed at the Institut de Cancérologie de l'Ouest (ICO) between December 2017 and February 2018.

## 2.2. Robot model development

The robotic system used in the current study was the *da Vinci* Si surgical system,<sup>2</sup> with four arms (manipulators), one for the endoscope and three for surgical tools. The three arms for surgical tools are referred to as ArmNo1, ArmNo2, and ArmNo3 in this paper.

Once the robot is docked to the patient in the operating room, only the movement of the actuated (controlled) joints influences manipulator performance during surgery.<sup>16</sup> Therefore, the robot model was represented by a simplified kinematic representation of the actuated joints of the Si manipulators based on the Denavit–Hartenberg convention (Fig. 7).<sup>33,34</sup> The relationship between the planar manipulator joint angles ( $\theta_6 - \theta_8$  in Fig. 7) and the coordinates of the end-effector (remote

center of motion, RCM) is described by the inverse kinematic (IK) equation:

$$\theta' = J^{-1}r' \quad (1)$$

In this equation,  $\mathbf{r}$  is a vector that represents the coordinates of the manipulator end-effector (RCM in Fig. 7),  $\theta$  is a vector for the joint angles, and  $J$  is the *Jacobian* matrix.

Optimal entry ports were defined relative to the patient-specific model and determined as the 3D points on the patient-specific model that provided the surgical tools maximum accessibility (or endoscope visibility) to the operative site. The operative site is assumed to be a sphere enclosing the entire target organ (i.e., uterus) (target volume in Fig. 8). Tilting and panning motions of the surgical tools at the entry ports create a conical volume inside the patient, the apex of which is located at the entry port while the cone contains the target volume. The relationship between the cone angle ( $\alpha$ ) and the radius of the sphere of the operative site ( $r$ ) is described by  $\tan(\alpha) = r/D$ , where  $D$  is the distance between the cone apex and the centroid of the sphere. To ensure that the surgical tool sweeps the entire sphere of the target

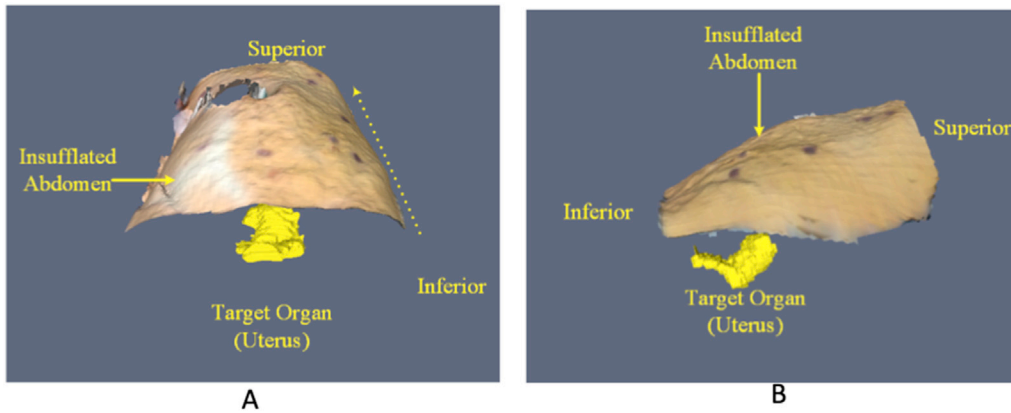


**Fig. 6** Example of a patient-specific model  
 A, Front view. B, Side view. The patient-specific model is the result of aligning the internal and external models. The patient-specific model is the 3D shape of the inflated abdomen (after insufflation), which includes the target organ uterus (in bright yellow).

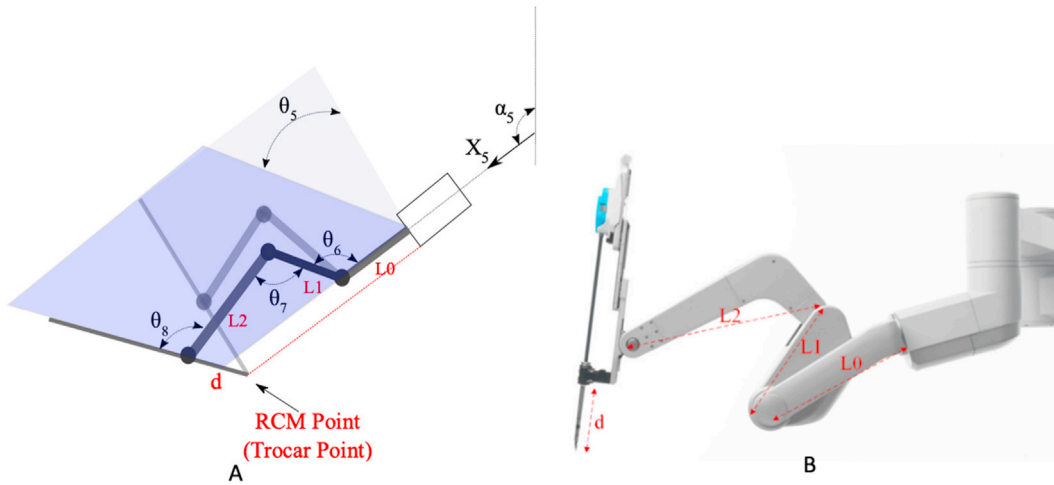


**Fig. 7** Robot model  
 A, A simplified kinematic representation of the actuated joints in the Si manipulators based on the Denavit–Hartenberg convention. B, da Vinci (Si) actuated joints with segment lengths labelled as L0, L1, and L2. The trocar length is labeled “d”. The planar motion of the Si manipulators at the trocar point (RCM) is created by joint angles ( $\theta_6 - \theta_8$  in A).

volume, an initial direction was chosen around which the surgical tool was supposed to rotate during surgery. This central direction is a line that connects the RCM at the entry port to the center of the target volume. If the surgical tool axis is represented by

normal vector  $\mathbf{n} (n_x, n_y)$ ,  $\mathbf{n}$  must be along the central direction. Accessibility of the entry ports on the patient model can be verified by solving the IK equation (1) with an additional constraint on the tool direction:

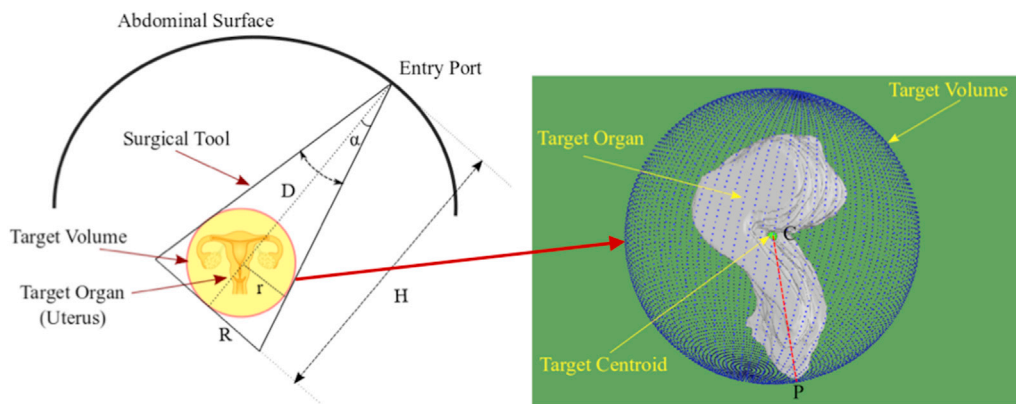


**Fig. 8** Target volume around the target organ in a hysterectomy procedure  
 The uterus (target organ) is considered to be enveloped by a spherical shape (target volume). During surgery, the surgical tool can pivot at the entry port and sweep the target volume. The radius of the target volume is the distance between the centroid of the target (C) and the farthest point of the target from the centroid (P).

$$x = L_0 \cdot \cos(\alpha_5) + L_1 \cdot \cos(\theta_6) + L_2 \cdot \cos(\theta_6 + \theta_7) + d \cdot \cos(\theta_6 + \theta_7 + \theta_8) \quad (2)$$

$$y = L_0 \cdot \sin(\alpha_5) + L_1 \cdot \sin(\theta_6) + L_2 \cdot \sin(\theta_6 + \theta_7) + d \cdot \sin(\theta_6 + \theta_7 + \theta_8) \quad (3)$$

$$n_x = \cos(\theta_6 + \theta_7 + \theta_8) \text{ or } n_y = \sin(\theta_6 + \theta_7 + \theta_8) \quad (4)$$

The unknown parameters in the above system of equations (2)–(4) are  $\theta_6$ ,  $\theta_7$ , and  $\theta_8$ .  $L_0$ ,  $L_1$ , and  $L_2$  are the robot (*da Vinci Si*) link lengths (see Fig. 7). The value “ $d$ ” is the trocar length, which is the distance between the entry point and robot end-effector. In equation (4), an additional constraint on the entry point was considered that keeps the surgical axis along the central direction that connects the entry point to the centroid of the target organ. Knowing the entry point coordinates on the patient-specific model  $\mathbf{r}(x, y)$ , the centroid of the target organ would be accessible via the selected port on the abdominal surface if at least one solution can be found for the system of equations (2)–(4). However, a necessary condition for solving the above equations is that the determinant of the Jacobean matrix in equation (1) is a nonzero value.<sup>19</sup> Otherwise, the problem has no solution for  $\theta_6$ ,  $\theta_7$ , and  $\theta_8$ . In other words, an arbitrary point on the abdominal surface (patient-specific model) satisfies the accessibility criterion for the robot manipulators, called an accessible point, if the determinant of the Jacobean matrix is not singular (nonzero).

### 2.3. Optimization algorithm for port placement

The port placement problem with input parameters can be defined as follows: Any four points on the patient-specific model can be identified as a set of potential entry port locations for the robot manipulators (including the endoscope arm). The optimization algorithm identifies the optimal port locations in the following steps.

#### 2.3.1. Check accessibility

The accessible points on the patient model are found by solving the IK equations (2)–(4) for each of the robot manipulators.

#### 2.3.2. Calculate the performance index

The manipulator performance index is calculated at every accessible point on the patient-specific model by using a performance index called manipulability,<sup>16,17,19</sup> defined as follows:

$$\begin{cases} \mathbf{w} = \sqrt{\det \mathbf{J}\mathbf{J}^T} & \text{for } m \neq n \text{ (redundant manipulator)} \\ \mathbf{w} = \det \mathbf{J} & \text{for } m = n \end{cases} \quad (5)$$

where  $\mathbf{w}$  is the manipulability index and  $\mathbf{J}$  is the Jacobean matrix.<sup>35</sup> Thus, for each of the manipulators, the calculated performance indices can be assigned to each of the accessible points on the abdominal surface.

#### 2.3.3. Select the preliminary points

The manipulability threshold is defined as  $T = \text{mean}(\text{accessible point manipulability}) + \text{standard deviation}(\text{accessible point manipulability})$  for each of the manipulators separately. Accessible points with manipulability indices greater than the threshold  $T$  are selected as preliminary entry ports. The preliminary points are labeled on the patient model as  $M(t_1)$ ,  $M(t_2)$ ,  $M(t_3)$ , and  $M(t_e)$ . The points  $M(t_i)$  and  $M(t_e)$  represent the highest manipulability region for the manipulator numbered  $i$  of the *da Vinci Si* model and the

endoscope arm, respectively. A sample of  $M(t_i)$  and  $M(t_e)$  is presented in Fig. 9.

#### 2.3.4. Determining the working volume of the surgical tools and endoscope

The working volume of the surgical tools and the field of view of the endoscope are defined inside the patient model as  $W_{t1}$ ,  $W_{t2}$ ,  $W_{t3}$ , and  $W_e$ , respectively. The working volume is a cone-shaped space with its apex located at the tool/endoscope entry port and the target volume within the cone (Fig. 8).

#### 2.3.5. Calculate the efficiency index for the preliminary points

Four points are selected from  $M_{t1}$ ,  $M_{t2}$ ,  $M_{t3}$ , and  $M_{te}$  to serve as the entry ports for the surgical tools and endoscope. The suitability of this set is evaluated by defining an efficiency index<sup>16,17</sup> as follows:

$$E(t_1, t_2, t_3, t_e) = \frac{\max(W_e \cup W_{t1} \cup W_{t2} \cup W_{t3})}{\max W_e} \quad (6)$$

$E$  is the ratio of the degree of manipulation to the endoscope arm's field of view. The efficiency index ranges from 0 to 1 and is to be maximized to find the optimal set of entry ports on the patient model.

#### 2.3.6. Internal collision prediction

Collision prediction is an algorithm for calculating the overlap between the working volumes of surgical tools through the selected ports in step 3. The measured overlap between each pair of working volumes inside the patient yields an internal collision index for each set of three manipulator entry ports:

$$C_{ij} = W_{ti} \cup W_{tj} \quad (7)$$

$C_{ij}$  is the collision index between the surgical tools pertaining to robot arms numbered  $i$  and  $j$ . For example,  $C_{12}$  is the collision value between the surgical tools that are connected to ArmNo1 and ArmNo2.

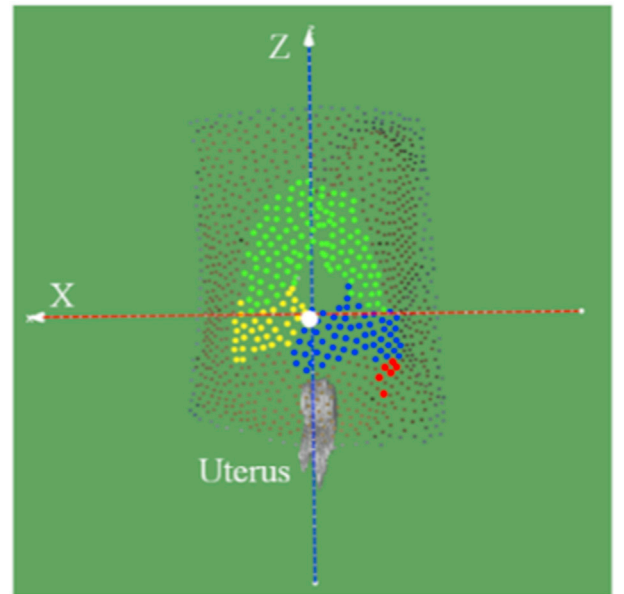


**Fig. 9** The first step in port location optimization Preliminary points for each port on the patient model:  $M(t_{11})$  in yellow,  $M(t_{12})$  in blue,  $M(t_{13})$  in red, and  $M(t_{1e})$  in green. The points  $M(t_i)$  and  $M(t_e)$  represent the highest manipulability region for the manipulator numbered  $i$  of the *da Vinci Si* model and the endoscope arm  $e$ .

### 2.3.7. Select optimal port placement

The preliminary points (obtained in step 3) are fed into an optimization function. A multi-objective optimization function,  $G(M_{ti})$ , is defined to select one or more sets of four points that maximize efficiency index  $E(t_1, t_2, t_3, t_e)$  while minimizing the collision indices ( $C_{ij}$ ) as follows:

$$G(M_{ti}) = G(E(t_1, t_2, t_3, t_e), C_{12}, C_{13}, C_{23}) \quad 1 \leq i \leq 4 \quad (8)$$

The “rPref” package of R software was used to find the Pareto front optimal solutions,  $G(M_{ti})$ , in equation (8).<sup>10,36,37</sup>

## 2.4. Verification of port placement optimization algorithm

### 2.4.1. Patient data collection

The algorithm described was applied in a test case for four patients undergoing robotic hysterectomy at ICO in France. CT images of patients were obtained before the procedure. For each patient, a patient-specific model of the abdomen was constructed as described above. Using the standard robot model, docking of the robot manipulators was simulated from different distances relative to the patient. To calculate the accessible points on the patient-

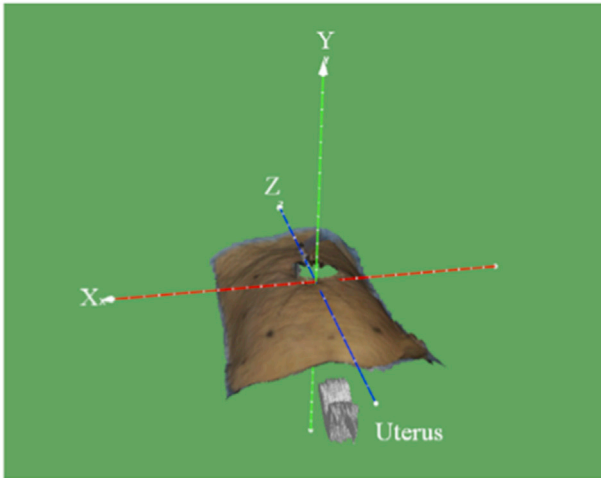


**Fig. 10** Reference frame for Patient 1

The reference frame is centered at the umbilicus. The Z-axis runs from the legs to the head, the X-axis runs from left to right, and the Y-axis runs from back to front.

specific model, a reference frame was defined with respect to the patient body, as illustrated for Patient 1 in Fig. 10. The Z-axis of the frame was along the direction from the patient's legs to the head, the X-axis was from left to right, and the Y-axis was from back to front. The center of the coordinate system was located on the umbilicus.

### 2.4.2. Optimal port placement determination

To find the optimal port locations, robot docking on the patient was simulated, and the positions of the first actuated joint on the robot arms were found in the reference frame, as shown in Fig. 11.<sup>38</sup> For a given manipulator position, the accessible points on the patient-specific model were found using the IK equations (2)–(4). MATLAB (MATrix LABORatory, The MathWorks, Inc.) was used to solve the IK problem for each of the manipulators. The number of IK equations for each manipulator depended on the number of 3D points on the patient-specific model. As the diameter of the trocars in robotic surgery ranges from 5 mm to 15 mm, a mesh simplification (clustering decimation) method<sup>39</sup> was used to eliminate points that were within this range in the generated patient-specific model.

### 2.4.3. Optimal robot position

The manufacturer's template for port-placement locations was used to determine the horizontal distance between robot manipulators (Fig. 12). According to these recommendations, the angle between the directions of the endoscope (B) and each of the arms, i.e., ArmNo1 (A), ArmNo2 (C) and ArmNo3 (D), must be at least 45° to prevent external collisions between the arms. Using these recommended angles in the X-Y plane, the minimum horizontal distance between the arms (along the x-axis in the reference frame to prevent external collisions) was calculated by:

$$X_A = L \times \sin(45^\circ), X_C = L \times \sin(45^\circ), X_D = L \times \sin(90^\circ) \quad (9)$$

$X_A$ ,  $X_C$ , and  $X_D$  are the X coordinates of the first active joints of ArmNo1, ArmNo2, and ArmNo3, respectively.  $L$  is the length of the actuated segment and is the same for all robot arms ( $L = 0.65$  m). In the above equation, it was assumed that the endoscope arm was positioned in the Y-Z plane along the mid-line of the patients' body ( $X_B = 0$ ). Therefore,  $X_A = 0.4596$  m,  $X_C = 0.4596$  m, and  $X_D = 0.65$  m according to equation (9). Based on these measures, there is no accessible point where the Y position of the endoscope arm is less than 30 cm or greater than 95 cm (Table 1). The maximum number

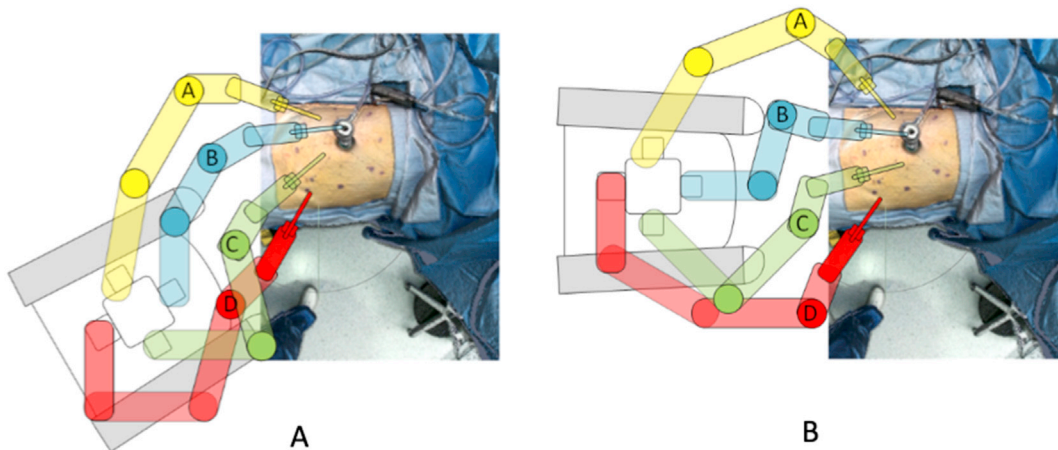


**Fig. 11** Robot docking in two different positions with respect to the patient

A, Docking at the side of the patient. B, Docking “between legs” of the patient. Simulation of the first actuated joint for robot arms (A = ArmNo1, B = endoscope, C = ArmNo2, and D = ArmNo3) can be found in the reference frame (see Fig. 10).



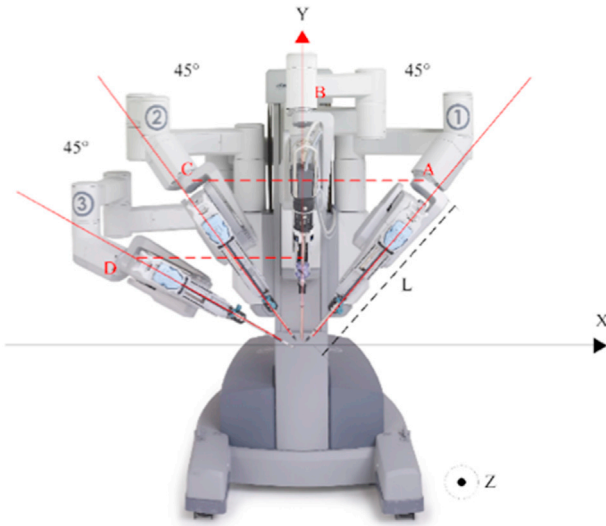


**Fig. 12** Manufacturer recommended angles between robot arms to avoid collision using the da Vinci Si Model

According to these recommendations, the angle between the directions of the endoscope (B) and each of the arms (ArmNo1 (A), ArmNo2 (C) and ArmNo3 (D)) must be at least 45° to prevent external collision between the arms. Using these recommended angles in the X–Y plane, the minimum horizontal distance between the arms (along the x-axis in the reference frame) is calculated to prevent external collisions.

of accessible points is 525, which belongs to the position of the endoscope at (X = 0.0, 0.45 ≤ Y ≤ 0.75, and Z = 0.0). The average manipulability index of accessible points was calculated for each position of the endoscope arm. The maximum value of the manipulability index was 0.198 (Table 1); this value was attained when the endoscope arm was positioned at (X = 0.0, Y = 0.75, and Z = 0.0).

**Table 1**  
Number of accessible points for the endoscope arm in different positions on Patient 1

x, m	y, m	z, m	Number of accessible points	Average of the manipulability index
<b>Endoscope position, (x = 0.0, 0.1 &lt; y &lt; 0.90, z = 0.0)</b>				
0.00	0.30	0.00	119	0.080504
0.00	0.35	0.00	222	0.071999
0.00	0.40	0.00	413	0.069685
0.00	0.45	0.00	525	0.082927
0.00	0.50	0.00	525	0.111749
0.00	0.55	0.00	525	0.14122
0.00	0.60	0.00	525	0.166539
0.00	0.65	0.00	525	0.185884
0.00	0.70	0.00	525	0.197547
0.00	0.75	0.00	525	0.197922
0.00	0.80	0.00	524	0.183885
0.00	0.85	0.00	499	0.154402
0.00	0.90	0.00	261	0.124962
0.00	0.95	0.00	6	0.0926
<b>Endoscope position, (x = 0.0, y = 0.75, -0.30 &lt; z &lt; 0.20)</b>				
0.00	0.75	-0.30	499	0.198359
0.00	0.75	-0.25	525	0.199308
0.00	0.75	-0.20	525	0.204729
0.00	0.75	-0.15	525	0.204673
0.00	0.75	-0.10	525	0.202175
0.00	0.75	-0.05	525	0.197922
0.00	0.75	0.00	525	0.191561
0.00	0.75	0.05	523	0.182515
0.00	0.75	0.10	509	0.172761
0.00	0.75	0.15	477	0.162807
0.00	0.75	0.20	425	0.154455

The optimal location for the endoscope arm in the Y direction can be determined based on either the number of available points in the patient-specific model or the average of the manipulability index. Here, the goal was to take both measures into account. Hence, Pareto front optimization<sup>36,37</sup> was used with these two objectives to find the optimal height of the endoscope arm. The Pareto front of these two objectives was a single point (X = 0.0, Y = 0.75, and Z = 0.0). Thus, the point y = 0.75 m (above the umbilicus) was selected as the optimal location of the endoscope in the Y direction. To determine the optimal position of the endoscope in the Z direction, the endoscope was positioned in the range of -0.30 ≤ z ≤ 0.20. The results of the accessible points with y = 0.75 m and -0.30 ≤ z ≤ 0.20 are shown in Table 1. Similarly, the optimal position of the endoscope in the Z direction was determined (z = -0.15 m in Table 1). A similar procedure was used to find the optimal positions of ArmNo1, ArmNo2, and ArmNo3 (Table 2).

Since more than one point exists on the Pareto fronts of ArmNo1, ArmNo2, and ArmNo3 (Table 2), a decision about the optimal location of ArmNo2 was made based on the manipulability index. The optimal positions of ArmNo1, ArmNo2, and ArmNo3 were 0.45 m, 0.45 m, and 0.15 m, respectively. Using the optimal Y position of the arms in Table 2, the optimal positions of ArmNo1, ArmNo2, and ArmNo3 were calculated as (0.46, 0.45, -0.10) (-0.46, 0.45, 0.00), and (-0.65, 0.15, -0.15), respectively. The accessible points on the patient-specific model for the optimal position of the endoscope, ArmNo1, ArmNo2, and ArmNo3 are shown in Fig. 13 (points in

**Table 2**  
Number of accessible points for ArmNo1, ArmNo2, and ArmNo3 in different positions for Patient 1

x, m	y, m	z, m	Number of accessible points	Average of the manipulability index
<b>ArmNo1 position (x = 0.46, 0.10 ≤ y ≤ 0.85, z = 0.0)</b>				
0.46	0.15	0.00	50	0.134924
0.46	0.20	0.00	249	0.138026
0.46	0.25	0.00	364	0.150586
0.46	0.30	0.00	471	0.158046
0.46	0.35	0.00	505	0.163559
0.46	0.40	0.00	492	0.16743
0.46	0.45	0.00	472	0.168515
0.46	0.50	0.00	444	0.16582
0.46	0.55	0.00	403	0.158617
0.46	0.60	0.00	332	0.150633
0.46	0.65	0.00	232	0.139372
0.46	0.70	0.00	58	0.122845
<b>ArmNo2 position (x = -0.46, 0.10 ≤ y ≤ 0.85, z = 0.0)</b>				
-0.46	0.15	0.00	40	0.125478
-0.46	0.20	0.00	239	0.136398
-0.46	0.25	0.00	367	0.14896
-0.46	0.30	0.00	485	0.155952
-0.46	0.35	0.00	515	0.162001
-0.46	0.40	0.00	499	0.166389
-0.46	0.45	0.00	479	0.168409
-0.46	0.50	0.00	452	0.16622
-0.46	0.55	0.00	410	0.161712
-0.46	0.60	0.00	351	0.151626
-0.46	0.65	0.00	239	0.13764
-0.46	0.70	0.00	57	0.122562
<b>ArmNo3 Position (x = -0.65, 0.00 ≤ y ≤ 0.85, z = 0.0)</b>				
-0.65	0.00	0.00	530	0.148852
-0.65	0.05	0.00	533	0.151069
-0.65	0.10	0.00	528	0.153136
-0.65	0.15	0.00	517	0.154335
-0.65	0.20	0.00	501	0.153912
-0.65	0.25	0.00	461	0.153388
-0.65	0.30	0.00	410	0.149613
-0.65	0.35	0.00	311	0.139683

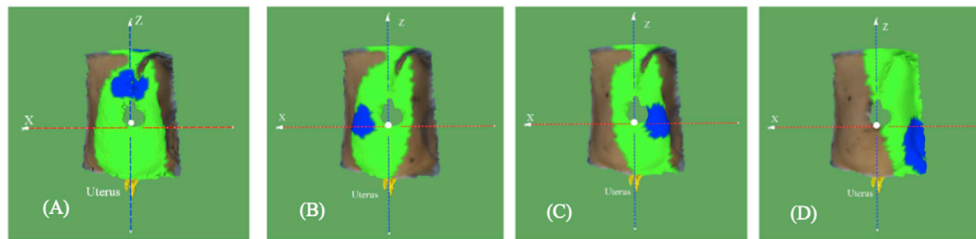


**Fig. 13** Determining accessible points for port placement in the optimization process for Patient 1

A, Accessible points (in green) and preliminary points (in blue) for the endoscope. B–D, Accessible points (in green) and preliminary points (in blue) for ArmNo1, ArmNo2, and ArmNo3.

green). Additionally, the preliminary points – the points with a manipulability index greater than the threshold (mean + standard deviation of the manipulability indices) – for each of the arms are highlighted in blue.

The above process was repeated for all four patients. The optimal positions of the manipulators and endoscope arm were calculated. The positions of the preliminary points for each of the robot manipulators and the endoscope were then fed into the optimization algorithm. The optimal locations of the ports were calculated to minimize internal collision between surgical tools and maximize the efficiency index in equation (6).

### 2.5. Face and construct validation

To validate the port-placement optimization system as a decision-aid, an expert review was conducted to obtain face and construct validity. Two experts, each with more than 20 years of experience and routinely performing hysterectomy procedures as a team using the da Vinci Robotic System, participated in the validation study. The validation process consisted of a demonstration of the system, followed by a hands-on trial of the system functionalities. Surgeons were encouraged to comment freely as they interacted with the system and provide specific feedback about how the system “appears to” perform the actual task of port location determination (face validity) and whether the system can perform the port placement task (construct validity). The work took place in the Brethen Center for Surgical Advancement in Robotics

and Minimally Invasive Surgery, located at Miami Valley Hospital in Dayton, Ohio, in June 2018.

### 2.6. Usability test

The usability test compared optimal port positions as determined by our optimization system to the actual ports determined by expert surgeons without the optimization tool. The study took place in the Brethen Center for Surgical Advancement in Robotics and Minimally Invasive Surgery, located at Miami Valley Hospital in Dayton, Ohio, from June to September 2018. The two expert surgeons who participated in the validation study also performed the usability test.

The usability study used the da Vinci Surgical System (Model Si) with a torso phantom to simulate the patient (Fig. 14). A small piece of soft plastic representing the target organ was placed in the phantom to simulate the uterus in a hysterectomy procedure. The target was placed on a cuboid that was attached to the base of the phantom by crisscrossing masking tape, simulating connective tissue to be ligated during surgery (Fig. 14C). Three different locations for the target organ were presented to the surgeons to simulate different organ displacements due to insufflation: in the center of the abdominal space, at the bottom of the torso along the midline, and in the bottom right corner of the torso, as depicted in Fig. 14D. Assuming the following coordinates of the robot when docked to the phantom: endoscope (0, 0.75, 0), ArmNo1 (0.46, 0.60, -0.10), and ArmNo2 (-0.46, 0.60, -0.10) (in meters) (Fig. 15),

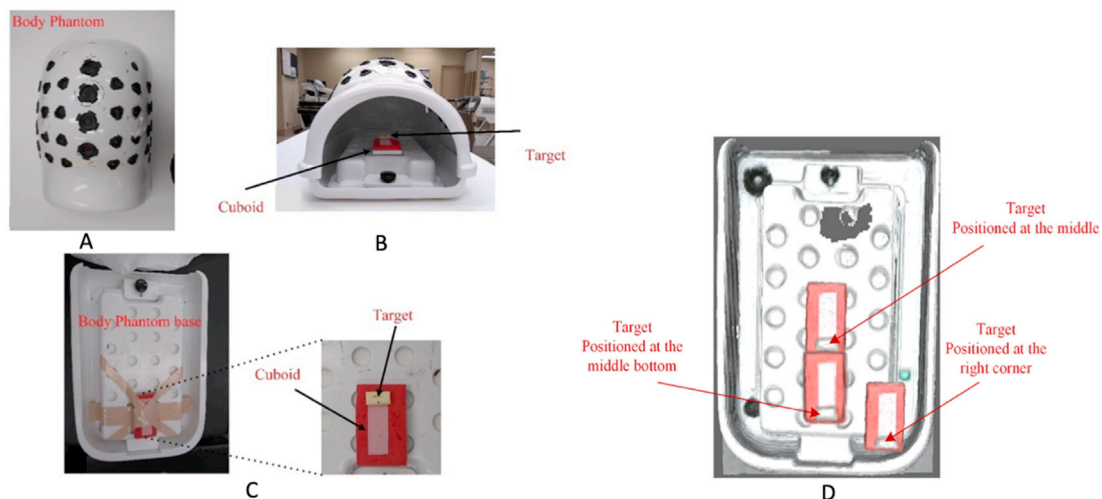


**Fig. 14** Torso phantom used in the usability test

A, Top view of the body phantom. B, Target placement in the phantom cavity. C, View of cuboid and target. D, Target placement in three different locations within the phantom to simulate different organ displacements due to insufflation.

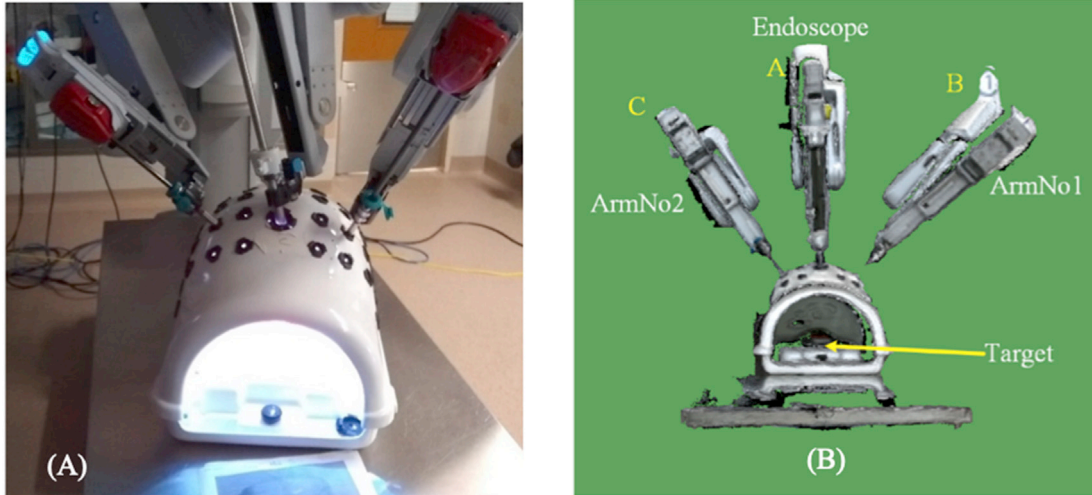


**Fig. 15** Experimental setup for validation and usability studies  
 A, The robot arms docked to the phantom torso. B, The positions of the endoscope, ArmNo1, and ArmNo2 relative to the phantom.

optimal port locations were calculated for each target position (Fig. 16A, B, C).

During the testing phase, expert surgeons were asked to determine the port locations for the robot arms as they would in a hysterectomy procedure for each of the three target locations or use the optimized ports as determined by the optimization system. Using the da Vinci robot with either port placement, surgeons performed the task of removing the 3 simulated target organs in the torso phantom. The task consisted of using a scissor tool to cut the tape that holds the cuboid in place in the torso phantom and using a grasper to pick up the target representing the uterus (Fig. 14C). The surgeon would first cut and peel the left part of the crisscrossed masking tape (X shape as shown in Fig. 14A and B), followed by the right part of the X-shaped tape. Finally, the surgeon peeled the center of the X-shaped tape away to reveal and remove the target, as shown in Fig. 14D.

Each surgeon performed all six conditions, in order from target 1 to target 3, alternating between their own port locations (actual ports) and optimized port locations as determined by the optimization algorithm on each target location.

**3. Results**

*3.1. Verification of port placement optimization algorithm*

The algorithm described was applied in a test case for 4 patients (ages ranged from 48 years to 70 years). Patient characteristics and CT image slices and the sizes of the acquisition matrices are presented in Table 3. After eliminating points, the number of points on each of the meshes was thus reduced by 92.85%–98.77% (Table 4).

The optimization algorithm was successfully verified on four patients following the same procedure. Fig. 17A presents an

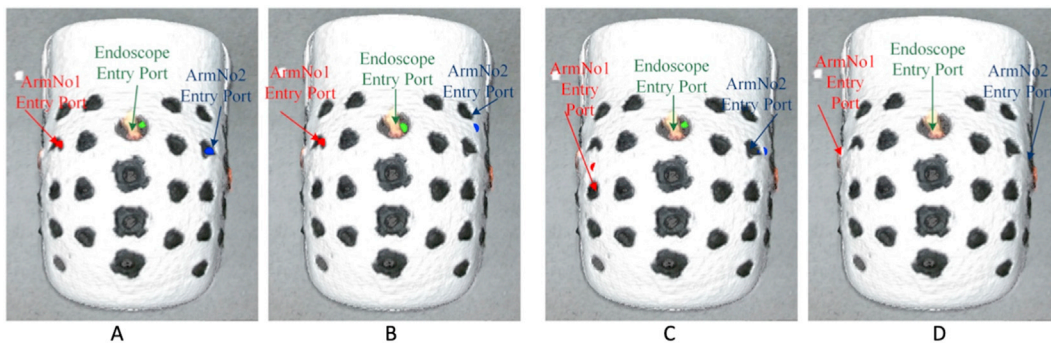


**Fig. 16** Optimized port locations for the target organ positioned in four different locations in the torso phantom, simulating organ displacements due to insufflation  
 A, Target organ in the right corner of the torso. B, Target organ in the middle of the torso. C, Target organ at the bottom of the torso. D, Actual port locations determined by the expert surgeons during the usability test.

**Table 3**  
 Patient characteristics and CT parameters

Patient label	Sex	Age, y	Weight, kg	Head-Body size, m	Number of slices	Acquisition matrix	Voxel spacing, (x, y, z), mm
Patient 1	F	59	58	1.65	562	512 × 512	0.68 × 0.68 × 1
Patient 2	F	48	55	1.63	319	512 × 512	0.61 × 0.61 × 1.25
Patient 3	F	63	70	1.71	426	512 × 512	0.97 × 0.97 × 2
Patient 4	F	70	63	1.68	249	512 × 512	0.62 × 0.62 × 2.5

**Table 4**  
Number of 3D points on the patient-specific models before and after mesh simplification

Patient label	Number of 3D points (before simplification)	Number of 3D points (after simplification)	Percent reduction, %
Patient 1	80,871	1008	98.75
Patient 2	69,226	851	98.77
Patient 3	13,432	947	92.95
Patient 4	12,901	922	92.85

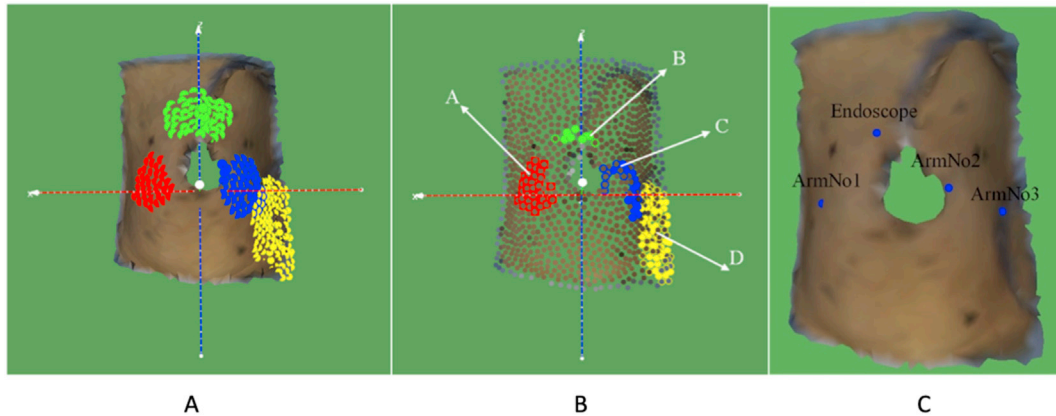


**Fig. 17** Pareto optimization solution in final port placement determination

A, The preliminary points for robot arms on the patient-specific model in Patient 1. The green points are for the endoscope, the red points are for ArmNo1, the blue points are for ArmNo2, and the yellow points are for ArmNo3. B, The Pareto optimization solution for optimal port locations yields four clusters of points that are the optimal positions for the endoscope, ArmNo1, ArmNo2, and ArmNo3, individually. From all possible combinations of the four colored points in B, the top ranking three combinations with the lowest collision index for ArmNo1-ArmNo2 are selected to determine the ArmNo1 location. Then, the ArmNo2 location is determined after filtering out the first two values that minimize collision between ArmNo2 and ArmNo3. C, ArmNo3 location is determined by the two remaining combinations that yield the minimum collision between ArmNo1 and ArmNo3.

integrated view of the preliminary points on the patient-specific model for all robot arms in Patient 1 (from Fig. 13). The green points are for  $M(t_e)$ , the red points for  $M(t_1)$ , the blue points for  $M(t_2)$ , and the yellow points for  $M(t_3)$ . Solving equation (8), the Pareto optimization solution for optimal port locations provided four clusters of points that are the optimal positions for the endoscope, ArmNo1, ArmNo2, and ArmNo3 (Fig. 17B).

The total number of combinations for the optimal positions of the endoscope, ArmNo1, ArmNo2, and ArmNo3 was 1490. Any subset of these 1490 optimal port positions can be selected as entry ports on the patient abdominal surface. For example, Fig. 17B presents one combination in which the port positions for ArmNo1, the endoscope, ArmNo2, and ArmNo3 are labeled A, B, C, and D, respectively. However, the number of solutions was restricted by choosing the entry ports in order. First, the endoscope entry port was determined, followed by the locations of the ports for ArmNo1, ArmNo2, and ArmNo3, sequentially. Four solutions (from 1490 combinations of the entry ports in Fig. 17B) with the highest efficiency index were selected to determine the endoscope port. From these four combinations, the first three combinations with minimum values of the collision index between ArmNo1 and ArmNo2 were selected to determine the ArmNo1 port location. Similarly, these three combinations were filtered by the first two values that minimize the collision between ArmNo2 and ArmNo3 to determine

the position of ArmNo2. Finally, from the two remaining combinations of the entry ports, the minimum collision between ArmNo1 and ArmNo3 was selected (ArmNo1, ArmNo2, ArmNo3, and the endoscope) to determine the position of ArmNo3 (Fig. 17C). The results of optimized port placement for Patients 2, 3, and 4 are presented in Table 5 and Fig. 18.

### 3.2. Face and construct validity

For face and construct validation, surgeons verified that the optimization tool appeared to perform the port placement task as in actual surgery; the optimized port locations were in the expected regions of the patient's abdominal surface; and the relative arrangements were correct. They also expressed satisfaction and comfort with the optimized port locations while performing the task.

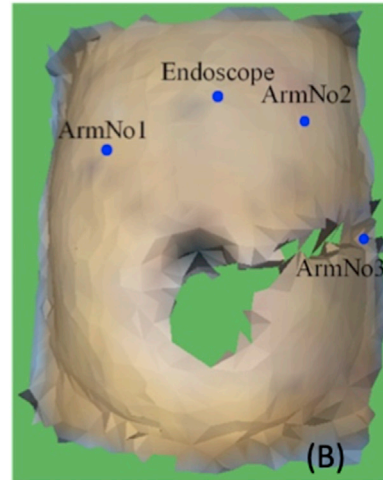
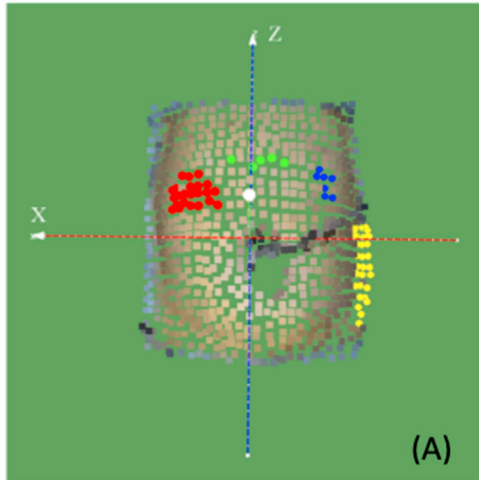
### 3.3. Usability test

The results of surgeons' performance based on the time to task completion are presented in Table 6. Consistently, the time to task completion using the optimized port locations was 28%–40% faster than the expert surgeons' port placement without the optimization tool.

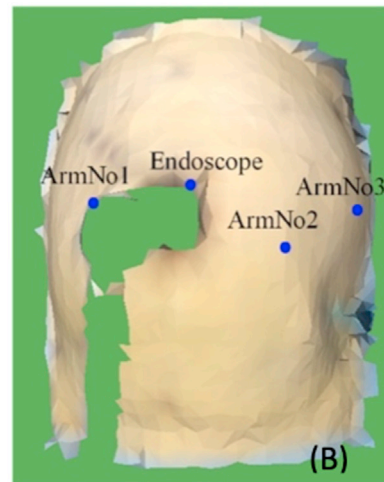
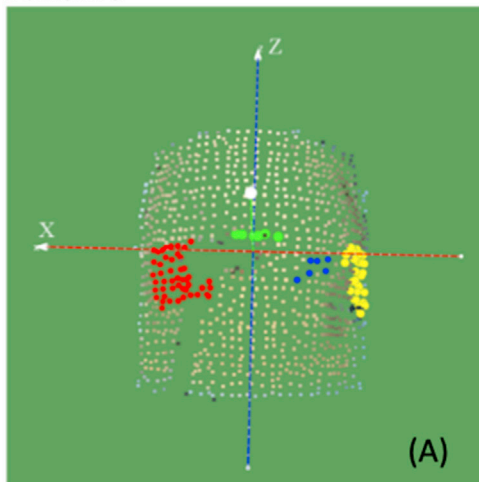
**Table 5**  
Optimal positions for robot arms in Patients 2, 3, and 4

Patient label	Endoscope opt. position, (x, y, z), m	ArmNo1 opt. position, (x, y, z), m	ArmNo2 opt. position, (x, y, z), m	ArmNo3 opt. position, (x, y, z), m
Patient 2	(0.0, 0.75, -0.20)	(0.46, 0.50, -0.30)	(-0.46, 0.50, -0.30)	(-0.65, 0.20, -0.05)
Patient 3	(0.0, 0.75, -0.20)	(0.46, 0.45, -0.30)	(-0.46, 0.45, -0.30)	(-0.65, 0.15, 0.00)
Patient 4	(0.0, 0.70, -0.30)	(0.46, 0.45, -0.30)	(-0.46, 0.40, -0.30)	(-0.65, 0.05, 0.00)

Patient 2



Patient 3



Patient 4

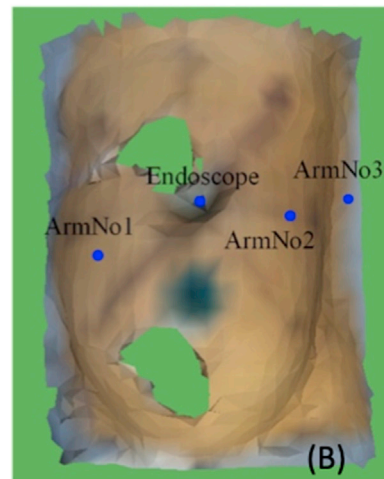
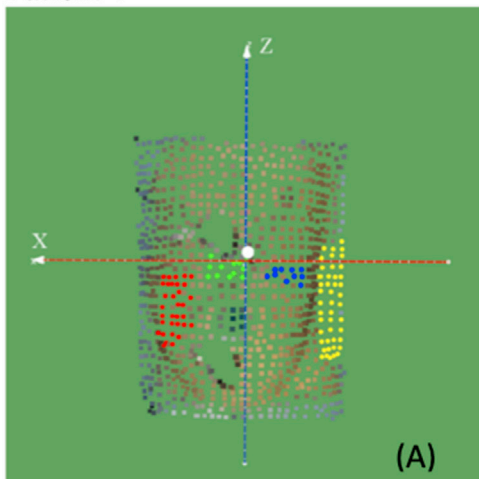


**Fig. 18** Pareto optimization solution for final port placement determination in Patients 2, 3, and 4  
 A, Optimal positions for robot arms. Green points are for the endoscope, red points are for ArmNo1, blue points for ArmNo2, and yellow points for ArmNo3. B, Optimized positions selected for maximum efficiency and minimum collision for the robot arms and the endoscope.

**Table 6**  
Time to task completion using the actual and the optimized ports

	Target Position 1 <sup>a</sup>		Target Position 2 <sup>b</sup>		Target Position 3 <sup>c</sup>	
	TA, min	TO, min	TA, min	TO, min	TA, min	TO, min
Surgeon 1	1.52	0.75	1.88	1.05	2.26	1.42
Surgeon 2	1.03	0.93	1.51	1.4	2.05	1.18
Mean $\pm$ SD	1.28 $\pm$ 0.35	0.84 $\pm$ 0.13	1.70 $\pm$ 0.26	1.23 $\pm$ 0.25	2.15 $\pm$ 0.15	1.30 $\pm$ 0.17
Mean TA- Mean TO	0.44		0.47		0.86	
Difference, %	34		28		40	

TA, time to task completion using actual ports determined by expert surgeons. TO, time to task completion using optimized ports determined by the optimization algorithm.

<sup>a</sup> Center of torso.

<sup>b</sup> Bottom midline of torso.

<sup>c</sup> Bottom right corner of torso.

#### 4. Discussion

Interestingly, during the port-placement step of the procedure, the two expert surgeons agreed on the same port locations for all three target positions. That is, the same ports were used to access all three targets by both surgeons. Surgeons indicated that port placement is always approximative and that adjustments in surgical manipulations are routine in their daily practice. Despite more than 20 years of experience in performing robot-assisted hysterectomy procedures, expert surgeons are not able to precisely account for the variations in the target positions within the patient's abdomen and pelvis. Rather, they rely on their expert surgical skills to compensate for any difficulties caused by suboptimal port locations, sometimes at the expense of prolonging the surgery and the time that patients are under anesthesia.

The efficiency gains of up to 40% in task performance using the optimized ports confirm that when ports are well placed, surgical tools can reach the target and manipulations are easier, resulting in a shorter time to complete the surgical task. The time saved can mean a reduction in fatigue for the surgeons and operating room staff, less anesthesia for the patient, lower costs per surgery and more procedures per day for the hospitals.

#### 5. Conclusion

The decision-aid, based on an individualized patient-specific model, robot model, and optimization algorithm, was shown to be effective at addressing the challenges of displaced organs due to insufflation in robot-assisted hysterectomy. The face and construct validity of the decision-aid was established by expert surgeons, while efficiency gains in task performance were demonstrated experimentally. Our development approach can be applied to other surgical procedures to reduce uncertainty and enhance surgical performance and outcome.

#### Author contributions

Study conception and design: Mohammad. R. Maddah, Caroline G. L. Cao. Imaging data acquisition and analysis: Jean-Marc Classe, Isabelle Jaffre. Model development: Mohammad. R. Maddah, Damien Chablat, Cedric Dumas. Algorithm development and verification: Mohammad. R. Maddah, Jean-Marc Classe, Isabelle Jaffre. Validation and usability studies: Mohammad. R. Maddah, Keith A. Watson, Katherine S. Lin. Manuscript draft and revision: Mohammad. R. Maddah, Cedric Dumas, Caroline G. L. Cao.

#### Conflict of interest

The authors declare no conflicts of interest.

#### Ethics approval

All applicable international, national, and/or institutional guidelines for responsible conduct of research with human subjects were followed. In accordance with law n°2012–300 (March 5, 2012) governing non-interventional clinical research in France, and its implementing decree n°2017–884 (May 9, 2017), this study did not require authorization from an ethics committee.

#### Consent from patients and participants

Data from four patients used to develop and verify the optimization algorithm were anonymized. The expert surgeons provided expert opinions for face and construct validation. In accordance with law n°2012–300 (March 5, 2012) governing non-interventional clinical research in France, and its implementing decree n°2017–884 (May 9, 2017), this study did not require written informed consent from the participants.

#### Funding

This work was supported in part by the Ohio Imaging Research and Innovation Network (non-restricted grant), the École des Mines de Nantes with a partial PhD grant, and Region Bretagne, FEDER and the University of South Australia for funding the Chair for Industry of the Future.

#### Acknowledgments

We thank the patients and healthcare providers for their participation.

#### References

1. Robotic surgical systems. DA Vinci. Intuitive. Accessed 29 April 2023. <https://www.intuitive.com/en-us>
2. Perrin M, Fletcher A. Laparoscopic abdominal surgery. *Con Educ Anaesth Crit Care Pain.* 2004;4(4):107–110.
3. Wang J, Lin KS, Keith AW, Galloway ML, Hellan M, Cao Caroline CGL. Need help with port-placement in robot-assisted surgery: a survey study. Accessed 29 April 2023. <https://www.sages.org/meetings/annual-meeting/abstracts-archive/need-help-with-port-placement-in-robot-assisted-surgery-a-survey-study/>
4. Coste-Manière È, Adhami L, Severac-Bastide R, et al. Optimized port placement for the totally endoscopic coronary artery bypass grafting using the da Vinci robotic system. In: Rus D, Singh S, eds. *Experimental Robotics VII.* Springer; 2002:199–208.
5. Coste-Manière È, Adhami L, Mourgues F, et al. Optimal planning of robotically assisted heart surgery: transfer precision in the operating room. In: Siciliano B, Dario P, eds. *Experimental Robotics VIII.* Springer; 2003:424–434.
6. Cestari A, Buffi NM, Scapaticci E, et al. Simplifying patient positioning and port placement during robotic-assisted laparoscopic prostatectomy. *Eur Urol.* 2010;57(3):530–533.

7. Song C, Alijani A, Frank T, Hanna GB, Cuschieri A. Mechanical properties of the human abdominal wall measured in vivo during insufflation for laparoscopic surgery. *Surg Endosc*. 2006;20(6):987–990.
8. Maddah MR, Dumas C, Gauthier O, Fusellier M, Cao CGL. Measuring organ shift and deformation for port placement in robot-assisted minimally invasive surgery. *Laparosc Endosc Robot Surg*. 2020;3(4):99–106.
9. Chiu AM, Dey D, Drangova M, Boyd WD, Peters TM. 3-D image guidance for minimally invasive robotic coronary artery bypass. *Heart Surg Forum*. 2000;3(3):224–231.
10. Sun LW, Yeung CK. Port placement and pose selection of the da Vinci surgical system for collision-free intervention based on performance optimization. In: *Proceeding of the 2007 IEEE/RSJ International Conference on Intelligent Robots and Systems*. IEEE; 2007:1951–1956.
11. Bañez J, Caro S, Schwaizberg S, Classe JM, Cao CGL. Modeling patients for optimized port placement in robot-assisted surgery. In: *In: Proceedings Of ASME 2012 11<sup>th</sup> Biennial Conference On Engineering Systems Design And Analysis*. The American Society of Mechanical Engineers; 2012:821–826.
12. Banez J. *Design and Evaluation of a Planning Aid for Port Placement in Robot-Assisted Laparoscopic Surgery*. Master's Thesis. Tufts University; 2012.
13. Bano J, Hostettler A, Nicolau SA, et al. Simulation of pneumoperitoneum for laparoscopic surgery planning. *Med Image Comput Comput Assist Interv*. 2012;15Part I(15):91–98.
14. Sánchez-Margallo FM, Moyano-Cuevas JL, Latorre R, et al. Anatomical changes due to pneumoperitoneum analyzed by MRI: an experimental study in pigs. *Surg Radiol Anat*. 2011;33(5):389–396.
15. Adhami L. *An Architecture for Computer Integrated Mini-Invasive Robotic Surgery: Focus on Optimal Planning*. Dissertation. Ecole des Mines de Paris; 2002.
16. Trejos AL, Patel RV, Ross I, Kiaii B. Optimizing port placement for robot-assisted minimally invasive cardiac surgery. *Int J Med Robot*. 2007;3(4):355–364.
17. Sun LW, Van Meer F, Schmid J, Bailly Y, Thakre AA, Yeung CK. Advanced da Vinci surgical system simulator for surgeon training and operation planning. *Int J Med Robot Comput Assist Surg*. 2007;3(3):245–251.
18. Cannon JW, Stoll JA, Selha SD, Dupont PE, Howe RD, Torchiana DF. Port placement planning in robot-assisted coronary artery bypass. *IEEE Trans Robot Autom*. 2003;19(5):912–917.
19. Yoshikawa T. *Foundations of Robotics: Analysis and Control*. MIT press; 1990.
20. Feuerstein M, Mussack T, Heining SM, Navab N. Intraoperative laparoscope augmentation for port placement and resection planning in minimally invasive liver resection. *IEEE Trans Med Imag*. 2008;27(3):355–369.
21. Siewerdsen JH, Moseley DJ, Burch S, et al. Volume CT with a flat-panel detector on a mobile, isocentric C-arm: pre-clinical investigation in guidance of minimally invasive surgery. *Med Phys*. 2005;32(1):241–254.
22. Yoo TS, Ackerman MJ, Lorensen WE, et al. Engineering and algorithm design for an image processing Api: a technical report on ITK—the Insight Toolkit. *Stud Health Technol Inf*. 2002;85:586–592.
23. Schroeder WJ, Martin KM, Lorensen WE. The design and implementation of an object-oriented toolkit for 3D graphics and visualization. In: *Proceeding of Seventh Annual IEEE Visualization*. IEEE; 1996:93–100.
24. Yushkevich PA, Piven J, Hazlett HC, et al. User-guided 3D active contour segmentation of anatomical structures: significantly improved efficiency and reliability. *Neuroimage*. 2006;31(3):1116–1128.
25. Edelsbrunner H, Mücke EP. Three-dimensional alpha shapes. *ACM Trans Graph*. 1994;13(1):43–72.
26. Maddah MR, Cao CGL. Application of the alpha shape method to visualize and analyze surgical motion. *Surg Sci*. 2017;8(11):464–480.
27. Song C, Alijani A, Frank T, Hanna G, Cuschieri A. Elasticity of the living abdominal wall in laparoscopic surgery. *J Biomech*. 2006;39(3):587–591.
28. 3D software from Artec 3D. Best 3D scanning solution. Accessed 29 April 2023. <https://www.artec3d.com/3d-software>
29. Kinect for Windows. Windows apps. Microsoft learn. Accessed 29 April 2023. <https://developer.microsoft.com/en-us/windows/kinect>
30. Newcombe RA, Izadi S, Hilliges O, et al. Kinectfusion: real-time dense surface mapping and tracking. In: *In: Proceeding of 2011 10th IEEE International Symposium on Mixed and Augmented Reality*. IEEE; 2011:127–136.
31. Smisek J, Jancosek M, Pajdla T. 3D with Kinect. In: Fossati A, Gall J, Grabner H, Ren X, Konolige K, eds. *Consumer Depth Cameras for Computer Vision: Research Topics and Applications*. Springer; 2013:3–25.
32. Klimchik A, Pashkevich A, Chablat D. CAD-based approach for identification of elasto-static parameters of robotic manipulators. *Finite Elem Anal Des*. 2013;75:19–30.
33. Freschi C, Ferrari V, Melfi F, Ferrari M, Mosca F, Cuschieri A. Technical review of the da Vinci surgical telemanipulator. *Int J Med Robot*. 2013;9(4):396–406.
34. Caenen JL, Angue JC. Identification of geometric and nongeometric parameters of robots. In: *In: Proceeding of IEEE International Conference on Robotics and Automation*. IEEE; 1990:1032–1037.
35. Kuo CH, Dai JS, Dasgupta P. Kinematic design considerations for minimally invasive surgical robots: an overview. *Int J Med Robot*. 2012;8(2):127–145.
36. R Core Team. R: A Language and Environment for Statistical Computing. R Foundation for Statistical Computing, Vienna, Austria. Accessed 29 April 2023. <https://www.r-project.org/>
37. Rooks P. rPref: database preferences and skyline computation. Accessed 11 May 2023. <https://www.p-rooks.de/rpref/>
38. Ferzli GS, Fingerhut A. Trocar placement for laparoscopic abdominal procedures: a simple standardized method. *J Am Coll Surg*. 2004;198(1):163–173.
39. Hoppe H. New quadric metric for simplifying meshes with appearance attributes. In: *In: Proceeding Of IEEE Visualization*. IEEE; 1999:59–510.